Nano Research

Open Access

Research Article

DNA-assembled Au nanodisk-nanorod architecture: An extended plasmonic Born–Kuhn model with tunable chiroptical activity

Zeyu Song[1,2], Yihao Zhou[2], Jinyi Dong[2] ✉, Xin Xu[3], Lizhi Jiao[3], Jun Song[3], Xiang Lan[3] ✉, and Qiangbin Wang[1,2] ✉

[1] *School of Physical Science and Technology, ShanghaiTech University, Shanghai 201210, China*
[2] *CAS Key Laboratory of Nano-Bio Interface, Division of Nanobiomedicine and i-Lab, Suzhou Institute of Nano-Tech and Nano-Bionics, Chinese Academy of Sciences, Suzhou 215123, China*
[3] *State Key Laboratory of Advanced Fiber Materials, Center for Advanced Low-dimension Materials, and College of Materials Science and Engineering, Donghua University, Shanghai 201620, China*

Cite this article: *Nano Research*, **2026**, *19*, 94908618. https://doi.org/10.26599/NR.2026.94908618

ABSTRACT: Controlled three-dimensional chiral arrangement of plasmonic nanocomponents is crucial for understanding emergent light-matter interactions but remains challenging, particularly for heterogeneous plasmonic nanoparticles with distinct shape anisotropy. Here, using an elaborately designed DNA assembly strategy, we constructed hybrid chiral plasmonic systems integrating gold nanodisks and nanorods. Chiroptical activity arises from the asymmetric lateral displacement between them, and the sign and intensity of the circular dichroism are determined by the number and handedness of the nanorod arrangements. We reveal that this chiroptical activity originates from selective plasmonic coupling between the in-plane resonance of the nanodisks and the longitudinal resonance of the nanorods, representing an experimental realization of an extended plasmonic Born−Kuhn model. This work opens new avenues in plasmonics and nanophotonics by providing a design paradigm for constructing complex chiral architectures.

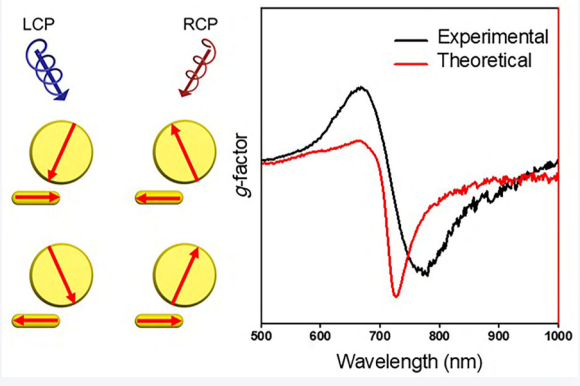

KEYWORDS: DNA origami, heterogeneous assemblies, gold nanodisk, chiral plasmonics, circular dichroism

1 Introduction

Chemical self-assembly of chiroplasmonic architectures aims to directionally organize nanoscale building blocks as "artificial atoms" toward macroscopic chiroptical activity through molecular-driven strategies [1–3], representing an indispensable approach for the precise fabrication of nanophotonic [4–6] and optoelectronic devices [7, 8]. This bottom-up approach is particularly crucial for constructing three-dimensional (3D) nanostructures, a task that remains challenging for conventional top-down techniques. To date, research in this field has predominantly relied on anisotropic metal nanoparticles such as gold nanorods (AuNRs) as basic building blocks. These materials endowed with strong plasmonic dipole moments along the longitudinal axis can generate significant chiroptical response upon controlled assembly [9–11]. Nevertheless, this AuNR-dominated paradigm inherently restricts structural diversity, resulting in well-established 3D oligomeric or polymeric structures such as helices [12, 13]. With increasing demand in applying the stereoscopic chiral configurations in flat integrated devices such as metasurface [14–18], realizing controllable assembly of planar-geometry nanoscale building blocks becomes crucial. In this context, anisotropic metal nanoparticles, for example, gold nanodisks (AuNDs) [19, 20] and gold nanoprisms [21–23], are promising candidates for expanding the planar chiral assembly. Their well-defined shapes are inherently compatible with patterned substrates, facilitating the transition of solution-phase chiral assembly techniques [24] to solid-state devices [25, 26]. More importantly, their distinct in-plane plasmon resonance [27] enables the construction of hybrid coupled systems, offering a platform for investigating complex chiral interactions in multicomponent plasmonic nanosystems [28]. However, achieving precise control over the chiral organizations with these emerging building blocks remains a great challenge.

Herein, through a delicate DNA origami [29–34] design approach, we realized a series of chiroplasmonic hybrid constructs

Received: January 27, 2026; **Revised:** March 3, 2026
Accepted: March 3, 2026

✉Address correspondence to Jinyi Dong, jydong2017@sinano.ac.cn; Xiang Lan, xlan@dhu.edu.cn; Qiangbin Wang, qbwang2008@sinano.ac.cn

through the orthogonal assembly of AuNDs and AuNRs at designated spatial positions. Both the number and handedness of AuNR arrangements were controlled at the periphery of an AuND core to explore the emergent chiral interactions between them. Our results reveal that the chiral arrangements of AuNRs relative to the AuND fundamentally determine the spectral sign of circular dichroism (CD), while the number of AuNRs nonlinearly modulates the signal intensities. We confirmed that the observed chirality originates primarily from the coupling between the longitudinal plasmon mode of the AuNRs and the in-plane plasmon mode of the AuNDs, demonstrating the realization of an extended plasmonic Born–Kuhn model [35–37]. The established experimental framework was further applied to realize even more sophisticated hybrids incorporating helical nanorods (HNRs) [38–41], revealing the interplay between local, intrinsic (HNR) [42] and collective (HNR-ND) chiral origins. Thus, these findings provide new insights into the complex chiral interactions in plasmonic nanosystems.

2 Experimental

2.1 Self-assembly, purification of DNA origami

For self-assembly of the DNA origami, 16 nM of the M13mp18 ssDNA scaffold strand and a staple mixture containing 320 nM of each staple strand were mixed in the folding buffer (pH = 8.0) containing 10 mM $MgCl_2$, 5 mM NaCl, 1 mM Tris-HCl, and 1 mM EDTA. The mixture was then annealed as follows: 80 °C for 8 min; from 75 to 27 °C, −1 °C/15 min; held at 27 °C. To remove the excess free staples and measure the concentration of DNA origami, the sample was mixed with 1×SYBR green dye, then purified by agarose gel electrophoresis (1%) in the ice bath at 70 V for 2 h. The gel was characterized by gel imager and the target bands were cut and chopped with a sharp knife on a sealing film to release the DNA origami. The sample solution was collected by extrusion with a thin cover glass. Then, the sample concentration was determined by measuring its absorbance at 260 nm.

2.2 Synthesis, functionalization, and assembly of the AuNRs/AuNDs with DNA origami

AuNRs were synthesized with dimensions of 27 × 5 nm [43] and 40 × 13 nm [44] using a seed-mediated growth method. AuNDs of 46 nm diameter were prepared following reported protocols [19]. HNRs were obtained by reacting AuNRs with L- or D-cysteine. Functionalization of the AuNRs/AuNDs/HNRs with thiolated DNA was carried out following the butanol dehydration method [45]. The AuNRs/AuNDs/HNRs functionalized with thiolated DNA were purified to remove excess free DNA strands by centrifugation and the pellets were redispersed in 0.02% SDS-0.5 × TBE buffer. The mixed sample and 300 μL of 0.02% SDS-0.5 × TBE buffer were added to the filter and centrifuged at 4000*g* for 1 min. The sample was washed five times by adding 400 μL of 0.02% SDS–0.5 × TBE buffer to the filter device for each rinse cycle until purification was complete. Finally, the filter was inserted upside down into a 0.5 mL tube and centrifuged at 4000*g* for 2 min to recover the purified sample solution. Purified DNA-functionalized AuNRs or HNRs were mixed with purified DNA origami at a 7:1 molar ratio. The concentration of functionalized AuNDs was calibrated by ultraviolet–visible (UV–Vis) absorbance (peak absorbance set to 18) and then mixed with 2.5 nM DNA origami solution at a 7:3 volume ratio. The mixture was annealed as follows: 45 to 30 °C, −1 °C/10 min; repeated for four cycles; held at 25 °C. The sample was purified by agarose gel electrophoresis (0.5%) in the ice bath at 70 V for 2 h. Then, the target bands were cut and squeezed into solution for characterizations.

The purified assemblies were then adsorbed onto the transmission electron microscopy (TEM) grids. The samples were characterized with TEM (Hitachi HT7700 TEM, 100 kV).

2.3 Spectroscopic characterization

The absorption spectra were recorded on a Thermo Scientific UV–Vis spectrometer. The CD spectra were acquired using an Applied Photophysics Chirascan-plus CD spectrometer. The assemblies were diluted in 0.5 × TBE-Mg^{2+} buffer, and CD spectra were collected from 500 to 1000 nm with a 1 cm path length, a scan speed of 100 nm/min, and under a nitrogen atmosphere.

The *g*-factor, also known as optical anisotropy factor, was calculated using

$$g = \frac{\text{CD (in mdeg)}}{33{,}000 \times \text{absorbance}}$$

3 Results and discussion

As shown in Fig. 1(a), a previously reported triangular DNA origami was employed as the assembly template [46]. This template contains designed binding sites for the site-specific attachment of AuNDs and AuNRs, enabling the construction of a double-layered chiral architecture (for DNA design, see Fig. S1 in the Electronic Supplementary Material (ESM)). The DNA origami measures 80 nm in edge length and approximately 2.5 nm in thickness, consisting of three identical secondary triangular sheets connected by fourteen DNA loops along each edge. For clarity, the face functionalized for AuNDs attachment is referred to as the top side, while the opposite face assembled with AuNRs is denoted as the bottom side.

Although extensive studies have reported DNA origami-mediated control of AuNR assemblies, it does not necessarily mean the success of applying the same designing concept based on DNA binding interactions to other complex nanoparticles or combination of heterogenous nanoparticles. In our study, to achieve precise positioning of the AuND, we first screened the AuND sizes and binding site distributions on the DNA origami. AuNDs of different sizes were assembled onto DNA origami templates carrying identical binding-site patterns. Three AuNDs (86, 66, 46 nm) were evaluated for geometric matching (Fig. 1(b)): (i) 86-nm AuNDs conform to the inscribed circle of the DNA origami, enabling full site coverage; (ii) 66-nm AuNDs, marginally undersized, maintain potential to all sites; (iii) and (iv) 46-nm AuNDs, although the smallest (Fig. S2 in the ESM), have a size that fits the densely arranged peripheral sites on the DNA origami. The assembly process was optimized by tuning the reaction ratio between AuNDs and thiolated DNA and by controlling the assembly sequence of AuNDs and AuNRs. These optimizations minimized structural aggregation and enabled high-yield formation of the target structures (Figs. S3–S5 in the ESM). Assembly precision was evaluated using TEM. Taking the three AuNR-AuND (ND-3NR) configurations as an example, positional accuracy was quantified by measuring the deviation between the center of each AuND and the geometric center defined by the three

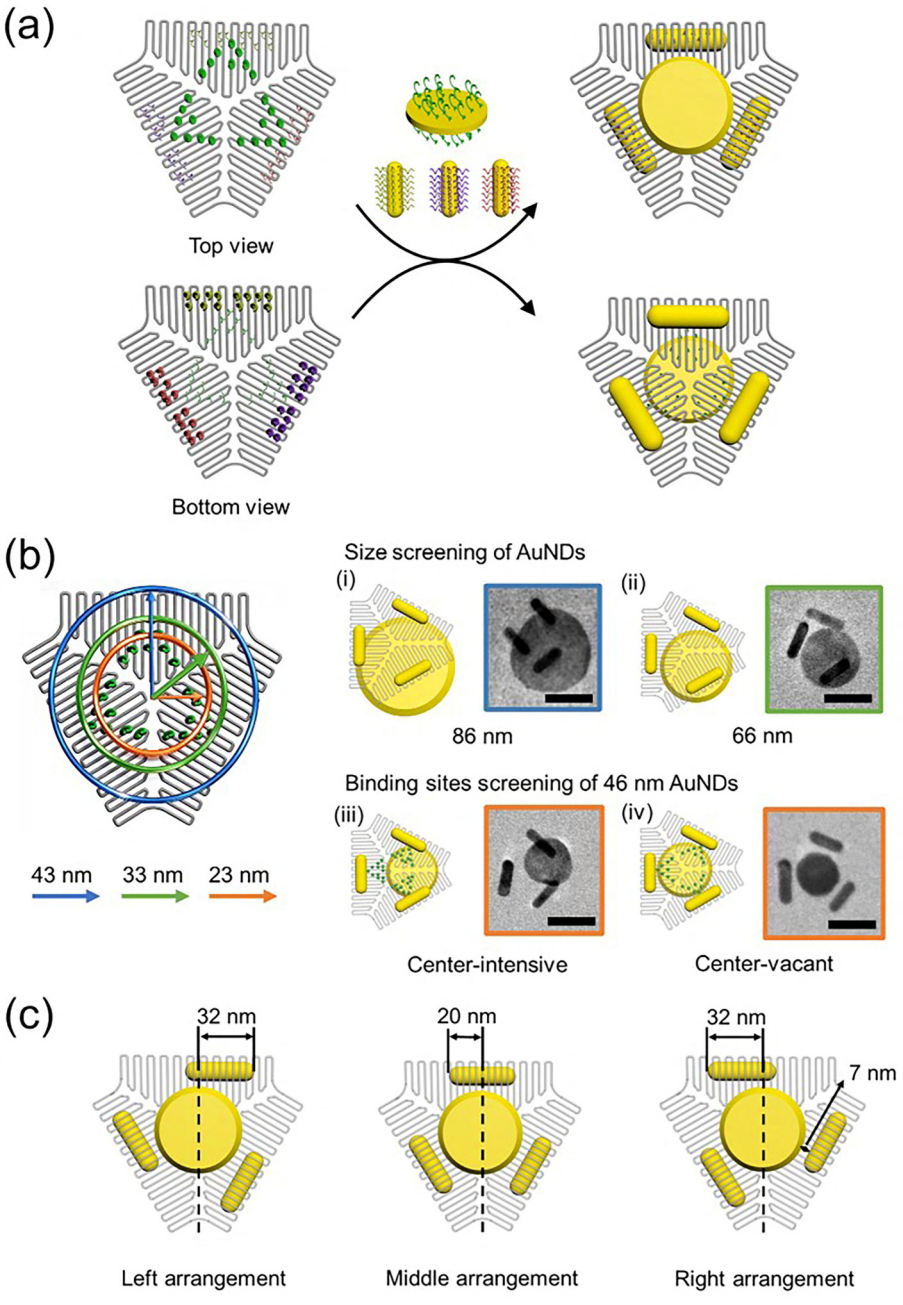

Figure 1 (a) Schematic diagram of heterogeneous assembly, showing a top view of DNA origami with AuNDs and a bottom view of DNA origami with AuNRs. (b) Size screening of AuNDs and binding sites analysis. Scale bar, 50 nm. (c) Arrangement of AuNRs on the structure at left, middle, and right positions relative to the central AuND core. The horizontal edge-to-edge distance between the AuNR and the AuND is 7 nm.

reference AuNRs. Both 86 and 66 nm AuNDs showed notable positional offsets, primarily due to their large effective binding area, which permits sufficient stability through partial hybridization of the binding sites without requiring strict center alignment. Further optimization showed that centrally clustered binding-sites create high local density, which can induce asymmetric local binding of the AuND, shifting it away from the center of the DNA origami (Fig. 1(b)(iii)). By rearranging sites into a peripherally concentrated pattern (Fig. 1(b)(iv)), this bias was avoided, achieving alignment between the AuND center and the structural center of the DNA origami [47]. To attach the AuNRs (40 × 13 nm), a strip of binding sites, each approximately 40 nm long, was patterned on each secondary triangular sheet at the bottom side of the DNA origami. The AuNR positions could be tuned by lateral shifting of the binding sites along the edge of the DNA origami (Fig. 1(c)). These design parameters enable the positional assembly of heterogeneous nanocomponents with tunable chirality.

In order to study the plasmonic interactions in the heterogeneous assemblies, we systematically tuned the number and chiral arrangement of AuNRs around the central AuND core. As shown in Figs. 2(a)–2(i), a series of AuNR-AuND architectures were successfully constructed. Precise control over the number and positions of AuNRs in each assembly was achieved by designing the specific binding sites, as depicted in Fig. S6 in the ESM. TEM

confirmed that the resulting structures matched the intended designs, with the AuND consistently centered within the AuNR arrangement and the spatial relationships closely following the expected geometries. We also quantified the assembly yields to evaluate the robustness of the approach. The binding efficiency of AuNDs to the DNA origami was high, as evidenced by the minimal number of structures lacking AuNDs (Fig. S7 and Table S1 in the ESM). Since the number and layout of binding sites are similar across different configurations, the R-ND-1/2/3NR was selected as a representative example for statistical analysis, as showed in Table S2 in the ESM. Analysis of approximately 100 structures per configuration showed that ND-1NR achieved a high yield of 87%, while yields for ND-2NR and ND-3NR remained considerable at about 57% (Fig. 2(j)), despite the increased complexity of incorporating multiple types of AuNRs. This controlled heterogeneous assembly strategy enables systematic investigation of the coupled chiral plasmonic responses arising from AuNR-AuNR and AuNR-AuND interactions.

The chiroptical activities in terms of *g*-factors were measured and compared for ND-1NR, ND-2NR, and ND-3NR structures, as well as for their corresponding mirror-image AuNR arrangements. First, we analyzed the *g*-factor spectra of ND-1NR structures (Fig. 3(a)). In the absence of the AuND, no CD signal was detected regardless of AuNR position, indicating that neither the AuNR itself nor its interaction with the DNA origami contributes measurably to the signals (Fig. S8 in the ESM). However, upon introducing the central AuND, significant CD signals emerged, showing a bisignate spectral lineshape peaked at 665 and 765 nm. The R-ND-1NR exhibited a dip-to-peak line shape, in which the peak at 765 nm was approximately twice as intense as that at 665 nm. Its mirror-image counterpart, L-ND-1NR, showed a reversed *g*-factor profile, confirming chiral inversion. The nominally achiral M-ND-1NR produced a small residual CD signal. Finite element method simulations support these observations (Fig. 3(b) and Figs. S9 and S10 in the ESM). A perfectly symmetric M-ND-1NR yields no signal, whereas R-ND-1NR and L-ND-1NR generate mirror-symmetric spectra with stronger peaks at longer wavelengths. The observed deviation in the M-ND-1NR signal likely results from the

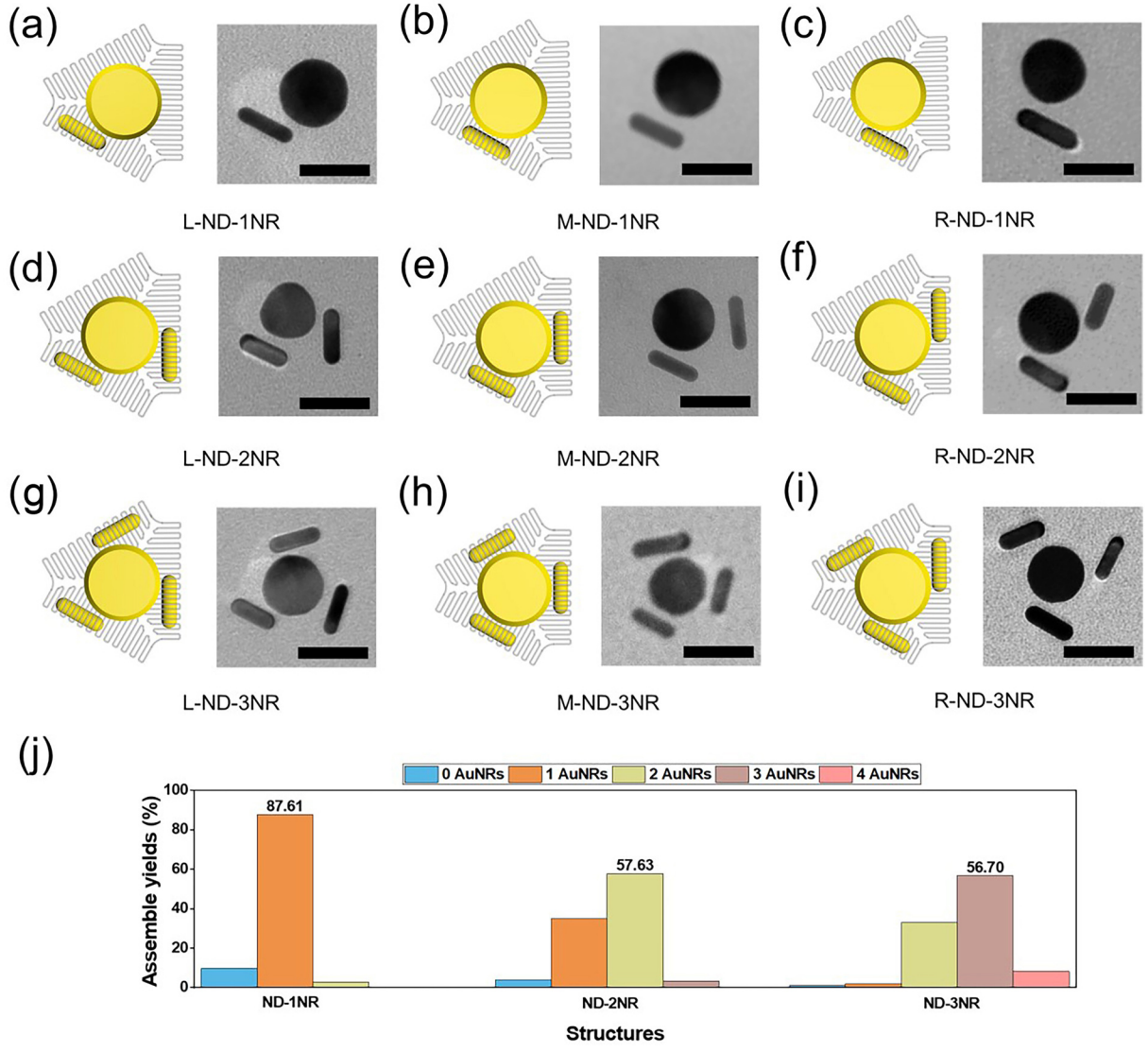

Figure 2 Schematic diagrams and TEM images of assemblies containing AuNDs and AuNRs with varied spatial arrangements. (a)–(c) Structures with one AuNR placed to the left (L), middle (M), and right (R) of the AuND core (L/M/R-ND-1NR). (d)–(f) Structures with two AuNRs (L/M/R-ND-2NR). (g)–(i) Structures with three AuNRs (L/M/R-ND-3NR). Scale bar, 50 nm (all panels). (j) Assembly yields for the different structures: ND-1NR (87.61%), ND-2NR (57.63%), and ND-3NR (56.70%).

intrinsic flexibility of the DNA origami and minor positional drift of the capture strands. Further simulation results indicate that these factors could collectively induce a slight rightward shift of the AuNR, as illustrated in Fig. S11 in the ESM. This same structural bias also explains why the CD signal of R-ND-1NR is stronger than that of its mirror-image counterpart, L-ND-1NR.

Unlike the single-AuNR case, assemblies containing only two or three AuNRs exhibited measurable CD signals (Figs. 3(c) and 3(e)), confirming that chiral coupling can arise among AuNRs alone. This observation aligns with previous reports on two-dimensional (2D) planar AuNR assemblies, where chirality originates from non-ideal planar orientations in solution [15]. Although AuNR-only assemblies generated detectable chiral signals, their intensities remained relatively low. However, upon incorporation of the AuND, the chiroptical behavior of the hybrid system changed significantly, matching the spectral line shapes predicted by simulation (Figs. 3(d) and 3(f)). Notably, all AuND-AuNR structures exhibited signal inversion compared to their AuNR-only counterparts, accompanied by a more than threefold increase in signal intensity. This can be explained by the dual role of the AuND. First, it promotes planarization of the assembly by fixing the flexible DNA origami scaffold (Fig. S12 in the ESM). Second, it acts as an electromagnetic coupling substrate, modulating and inverting the optical response of the hybrid structure, as illustrated in Figs. S13 and S14 in the ESM. The synergy of these two effects accounts for the observed signal enhancement and inversion. In addition, the CD peaks of the ND-2/3NR enantiomers are more symmetric than those of ND-1NR. We attribute this to the increased number of AuNRs, which renders the overall structure more planar and consequently leads to a more symmetric chiral configuration.

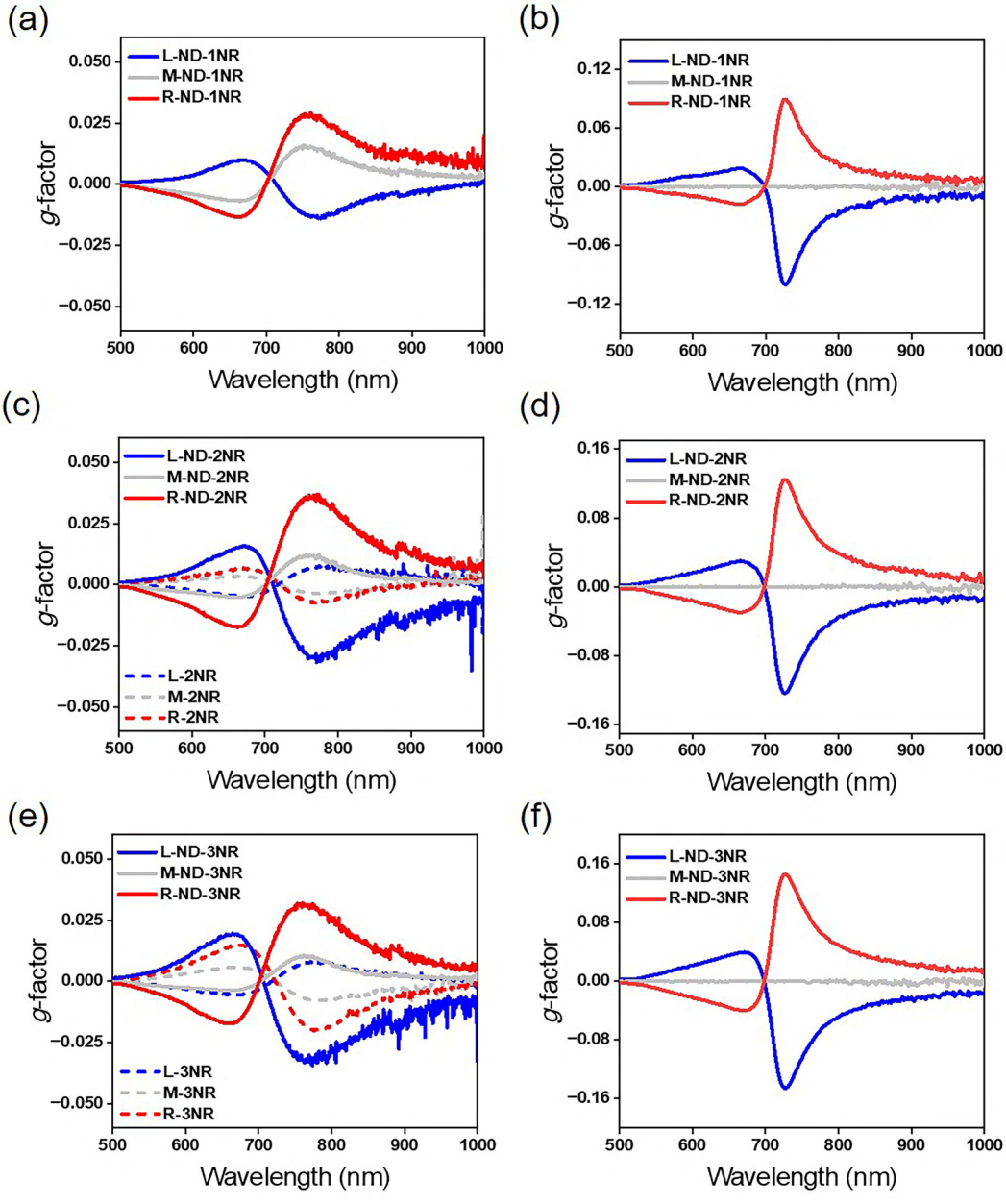

Figure 3 Experimental ((a), (c), and (e)) and simulated *g*-factor spectra ((b), (d), and (f)) for structures with varying numbers of AuNRs at different positions on the DNA origami. Experimental results are shown for configurations both with and without the central AuND core.

To elucidate the origin of the chiroptical properties of the AuNR-AuND hybrids, we simulated their polarization behavior under incident light in the *x*/*y*/*z* directions. Taking L-ND-1NR as an example, its surface charge distribution was displayed in Fig. 4(a). Under left-handed circularly polarized (LCP) and right-handed circularly polarized (RCP) light excitations in the *z* direction, the dipolar plasmonic resonances of AuNR and AuND are most prominent. The surface charge distribution corresponds to excitation of the in-plane dipole resonance of the AuND [48–50], and its orientation is defined relative to the longitudinal dipole of the AuNR. At 672 nm, the plasmonic interaction between the AuND and AuNR forms an antibonding-like mode, whereas at 722 nm it produces a bonding-like coupled mode. These wavelengths align with the resonant absorption wavelengths of AuND (672 nm) and AuNR (722 nm), respectively (Fig. 4(b)). At 672 nm, the coupled structure absorbs LCP light more strongly than RCP light, producing a positive CD signal, whereas the opposite occurs at 722 nm, yielding a negative signal. This results in a bisignate CD spectrum, a phenomenon also observed for L-ND-2/3NR. Further simulations reveal that L-ND-1/2NR exhibit right-handed CD spectra under *x*-incidence and left-handed CD spectra under *y*- and *z*-incidences (Fig. 4(c)), while L-ND-3NR generates left-handed signals in all incident directions (Figs. S15–S17 in the ESM). The CD signal intensity is the strongest for the *z*-incidence (black dashed line), which is consistent with the observation of the most prominent charge polarization effects under excitation in this direction.

To better explain the plasmonic coupling between the AuNR and AuND, we analyzed the ND-1NR system using the classical Born–Kuhn coupled-oscillator model (Fig. 4(d)). In this analogy, each component acts as a polarization-selectively excited dipole. In the established plasmonic Born–Kuhn model composed of two AuNRs, the D- and L-enantiomers are known to produce right- and left-handed CD signals, respectively [51]. A similar chiral interaction occurs in our structure under circularly polarized light excitations, mediated by the in-plane dipole of the AuND and the longitudinal dipole of the AuNR. Consequently, the L-ND-1NR configuration, analogous to the L-enantiomer of two AuNRs,

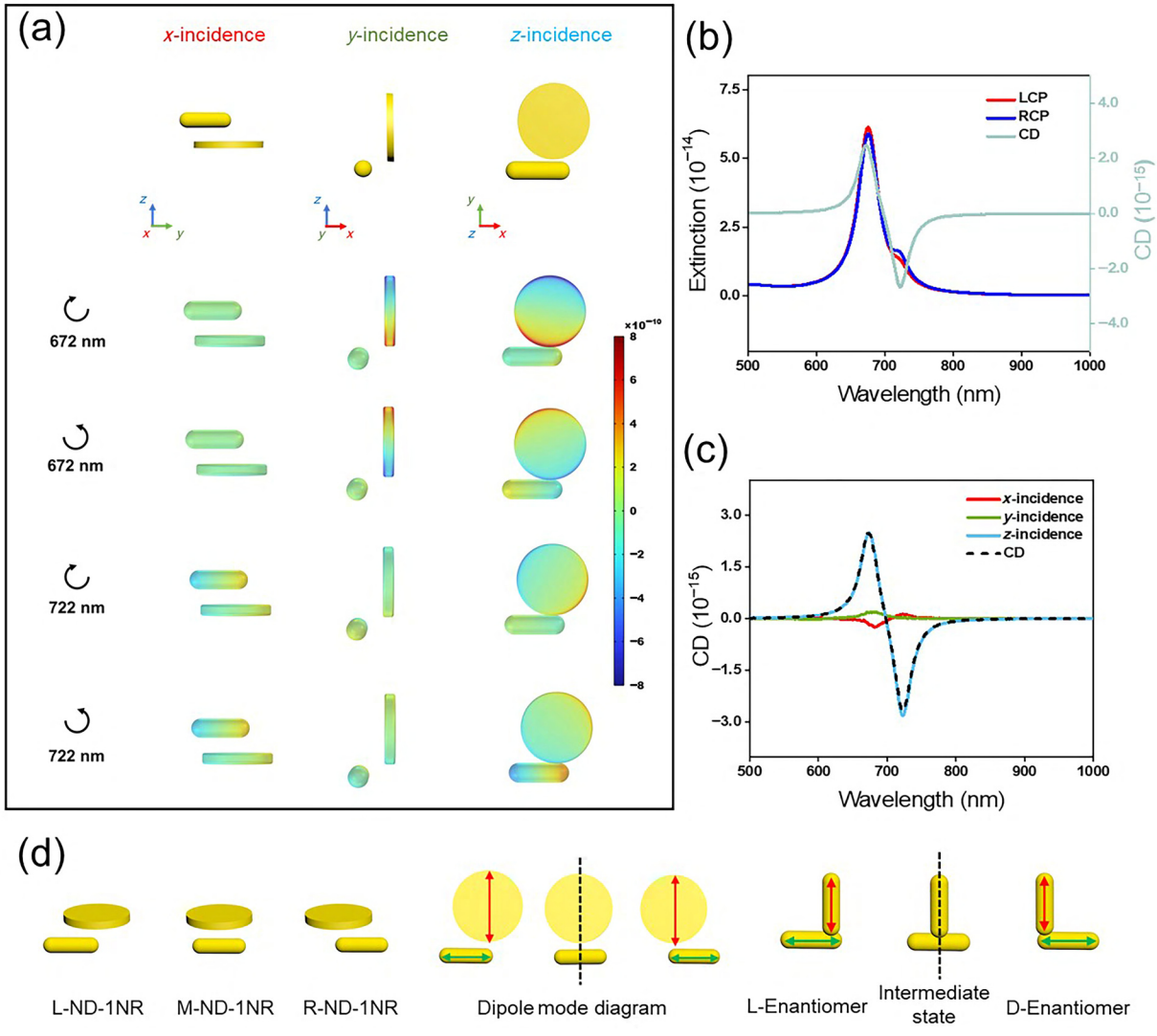

Figure 4 (a) Simulated surface charge distribution of the L-ND-1NR at 672 and 722 nm under *x*-, *y*-, and *z*-polarized incident light. (b) Simulated extinction spectra under LCP and RCP light and the corresponding CD spectrum of the L-ND-1NR. (c) Simulated extinction spectra under *x*-, *y*-, and *z*-polarized incident light and the resulting CD spectrum of L-ND-1NR. (d) A classical two-oscillator Born–Kuhn model illustrating the plasmonic coupling in the assembly composed of an AuND and an AuNR.

exhibits a left-handed bisignate CD response (Fig. S18 in the ESM). Conversely, R-ND-1NR behaves like the D-enantiomer, yielding a reversed CD signal. Thus, our AuNR-AuND architectures constitute an experimental realization of extended plasmonic Born–Kuhn model, potentially offering new insights into the physical design of sophisticated chiroptical systems.

The above studies provide a versatile platform to investigate complex chiral interactions among heterogeneous nanocomponents. As a further proof of concept, we constructed a new hybrid system comprising AuNDs and chiral HNRs with dimensions comparable to those of the achiral AuNRs (Figs. 5(a)–5(d) and Fig. S19 in the ESM). The *g*-factor spectra of DHNRs and LHNRs displayed mirror-symmetric profiles, featuring a strong peak near 550 nm and a weaker signal at long wavelengths. After introducing the AuNDs, a sharp bisignate signal emerged around 685 nm. As shown in Figs. 5(e) and 5(f), R-ND-LHNR and R-ND-DHNR exhibited a clear right-handed bisignate (dip-to-peak) signal near 685 nm, while L-ND-LHNR and L-ND-DHNR yielded only a very weak left-handed (peak-to-dip) response. This trend aligns with the results described above from ND-NR structures, indicating strong chiral coupling between the two components. The characteristic HNRs peak at 550 nm remains present, indicating that the overall chiroptical signal results from the superposition of the intrinsic HNRs signal and the contribution from HNR-ND coupling. This behavior persists even when the assembly yields vary across different sample types. As shown in Figs. S20–S22 in the ESM, we also fabricated assemblies with two and three HNRs, for assemblies containing only HNRs, increasing the number of HNRs did not significantly alter the spectral shape but slightly enhanced the *g*-factor intensity, indicating the presence of HNR–HNR coupling. In the presence of the AuND, a similar bisignate signal appeared around 685 nm, indicating contributions from the AuND plasmon resonance and the resulting HNR–ND coupling. These results clearly demonstrate the multiple origins of chirality in these structures, which include the intrinsic chirality of the HNRs as well as the collective chiral interactions arising from HNR–HNR and HNR–ND coupling.

4 Conclusions

In conclusion, we demonstrated chiral coordinated organization of heterogeneous and highly anisotropic plasmonic "artificial atoms", namely AuNRs and AuNDs, through a delicate DNA assembly strategy, and systematically investigated their chiroptical behaviors and modulation mechanisms. A series of structurally precise hetero-assemblies were constructed, establishing clear relationships

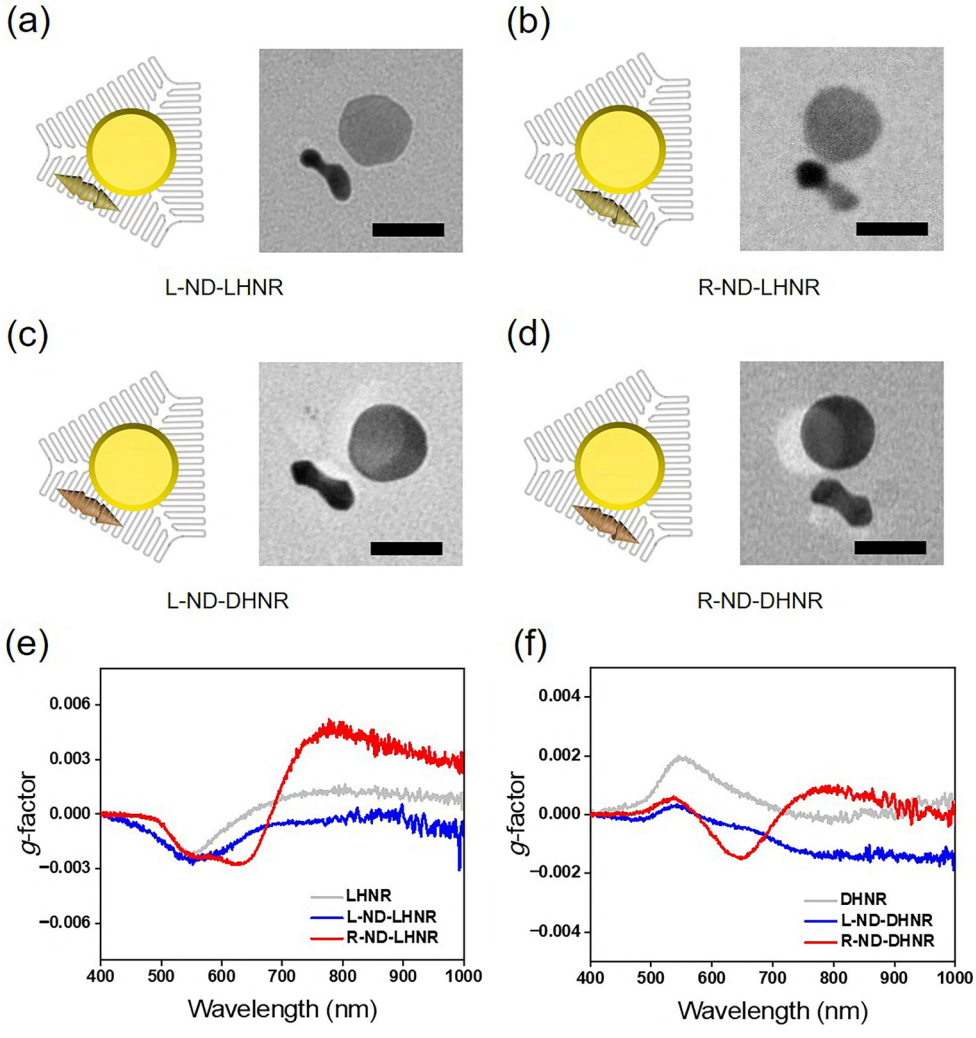

Figure 5 (a)–(d) Representative TEM images of the L-ND-LHNR, R-ND-LHNR, L-ND-DHNR, and R-ND-DHNR structures. Scale bar: 50 nm. (e) and (f) Corresponding *g*-factor spectra for these four configurations, with either LHNR or DHNR.

between the spatial arrangements of AuNRs (number and handedness) around the AuND core and the resulting chiral optical properties. Furthermore, by incorporating chiral HNR components, we created composite systems governed by coupled interactions arising from both interparticle chiral coupling (HNR–HNR, HNR–ND) and the intrinsic chirality of the HNRs. This strategy expands the diversity of self-assembled chiral plasmonic architectures through the integration of planar nanoscale building blocks. The developed chiral hybrid systems not only deepen the understanding of complex chiroptical phenomena, but also provide a combined theoretical and experimental foundation for the design and realization of more sophisticated nanoarchitectures toward integration into advanced metasurface photonic devices.

Electronic Supplementary Material: Supplementary material (additional TEM images of AuND/AuNR superstructures, DNA design details and sequences, and simulations) is available in the online version of this article at https://doi.org/10.26599/NR.2026.94908618.

Data availability

All data needed to support the conclusions in the paper are presented in the manuscript and the Electronic Supplementary Material. Additional data related to this paper may be requested from the corresponding author upon request.

Acknowledgements

This work was financially supported by the National Natural Science Foundation of China (Nos. 21934007, 22302227, and 22372031), the Strategic Priority Research Program of the Chinese Academy of Sciences (No. XDB36000000), the China Postdoctoral Science Foundation (No. 2022M712325), the Natural Science Foundation of Jiangsu Province (No. BK20230232), and the Jiangsu Funding Program for Excellent Postdoctoral Talent.

Declaration of competing interest

All the contributing authors report no conflict of interests in this work. Author Qiangbin Wang is the editorial board member of this journal, but he is not involved in the peer-review or decision of this article.

Author contribution statement

Z. Y. S.: Data curation, experimental design, validation, writing manuscript. J. Y. D.: Theoretical analysis, experimental design, writing – review and editing. Y. H. Z.: Formal analysis and discussion. X. X., L. Z. J., and J. S.: Discussion, validation. X. L.: Writing manuscript, funding acquisition, project administration. Q. B. W.: Funding acquisition, project administration, experimental design. All the authors have approved the final manuscript.

Use of AI statement

During the preparation of this work, the authors used DeepSeek-R1 671B (https://chat.deepseek.com) in order to polish the language. After using this tool/service, the authors reviewed and edited the content as needed and take full responsibility for the content of the publication.

References

[1] Querejeta-Fernández, A.; Chauve, G.; Methot, M.; Bouchard, J.; Kumacheva, E. Chiral plasmonic films formed by gold nanorods and cellulose nanocrystals. *J. Am. Chem. Soc.* **2014**, *136*, 4788–4793.

[2] Fan, Y. Q.; Fang, Y. X.; Che, S. N.; Zhang, W. N. Self-assembly of chiral mesostructured AIEgens-silica nanotubes with optical activities. *Nano Res.* **2025**, *18*, 94907676.

[3] Chen, Z.; Lin, T.; Li, H. H.; Sun, M. Z.; Su, C. L.; Huang, B. L.; Loh, K. P. Chiral self-assembly of terminal alkyne and selenium clusters organic-inorganic hybrid. *Nano Res.* **2022**, *15*, 2741–2745.

[4] Martens, K.; Funck, T.; Santiago, E. Y.; Govorov, A. O.; Burger, S.; Liedl, T. Onset of chirality in plasmonic meta-molecules and dielectric coupling. *ACS Nano* **2022**, *16*, 16143–16149.

[5] Wu, Z. H.; Wu, Z. M.; Lv, H. R.; Zhang, W. B.; Liu, Z. K.; Zhang, S.; Mu, E. Z.; Lin, H. X.; Zhang, Q.; Cui, D. X. et al. Nanophotonic catalytic combustion enlightens mid-infrared light source. *Nano Res.* **2023**, *16*, 11564–11570.

[6] Zhang, D.; Gao, X. Y.; Lu, J. J.; Lu, P.; Deitz, J.; Shen, J. N.; Dou, H. Y.; He, Z. H.; Shang, Z. X.; Wade, C. A. et al. Novel self-assembled two-dimensional layered oxide structure incorporated with Au nanoinclusions towards multifunctionalities. *Nano Res.* **2023**, *16*, 1465–1472.

[7] Xu, L.; Wang, W. X.; Li, Y.; Lin, Y. H.; Yue, W. J.; Qian, K.; Guo, Q. L.; Kim, J.; Shen, G. Z. N:ZnO/MoS_2-heterostructured flexible synaptic devices enabling optoelectronic co-modulation for robust artificial visual systems. *Nano Res.* **2024**, *17*, 1902–1912.

[8] Lin, Y. H.; Pan, J. Y.; Zhuang, X. M.; Guo, Q. K.; Li, Y. Integration of optoelectronic synapses and optical perception in MoS_2/WO_3 heterojunction for neuromorphic computing and visual bionic systems. *Nano Res.* **2025**, *18*, 94907660.

[9] Chen, Z.; Choi, C. K. K.; Wang, Q. B. Origin of the plasmonic chirality of gold nanorod trimers templated by DNA origami. *ACS Appl. Mater. Interfaces* **2018**, *10*, 26835–26840.

[10] Shen, C. Q.; Lan, X.; Lu, X. X.; Ni, W. H.; Wang, Q. B. Tuning the structural asymmetries of three-dimensional gold nanorod assemblies. *Chem. Commun.* **2015**, *51*, 13627–13629.

[11] Chen, Z.; Lan, X.; Chiu, Y. C.; Lu, X. X.; Ni, W. H.; Gao, H. W.; Wang, Q. B. Strong chiroptical activities in gold nanorod dimers assembled using DNA origami templates. *ACS Photonics* **2015**, *2*, 392–397.

[12] Cheng, G. Q.; Xu, D.; Lu, Z. Y.; Liu, K. Chiral self-assembly of nanoparticles induced by polymers synthesized via reversible addition-fragmentation chain transfer polymerization. *ACS Nano* **2019**, *13*, 1479–1489.

[13] Lu, J.; Xue, Y.; Bernardino, K.; Zhang, N. N.; Gomes, W. R.; Ramesar, N. S.; Liu, S. H.; Hu, Z.; Sun, T. M.; De Moura, A. F. et al. Enhanced optical asymmetry in supramolecular chiroplasmonic assemblies with long-range order. *Science* **2021**, *371*, 1368–1374.

[14] Liu, Y.; Ma, L.; Jiang, S. X.; Han, C.; Tang, P.; Yang, H.; Duan, X. Y.; Liu, N.; Yan, H.; Lan, X. DNA programmable self-assembly of planar, thin-layered chiral nanoparticle superstructures with complex two-dimensional patterns. *ACS Nano* **2021**, *15*, 16664–16672.

[15] Ma, L.; Liu, Y.; Han, C.; Movsesyan, A.; Li, P. H.; Li, H. C.; Tang, P.; Yuan, Y. Q.; Jiang, S. X.; Ni, W. H. et al. DNA-assembled chiral satellite-core nanoparticle superstructures: Two-state chiral interactions from dynamic and static conformations. *Nano Lett.* **2022**, *22*, 4784–4791.

[16] Dong, B. Q.; Xu, X.; Guan, R. C.; Jiang, S. X.; Ma, L.; Hu, H. T.; Ke, Y. G.; Liu, N.; Lan, X. Two-dimensional, chiral colloidal superlattices engineered with DNA origami. *Nano Lett.* **2025**, *25*, 5705–5712.

[17] Dong, B.; Zu, H. R.; Song, R. G.; Luo, Z.; Qian, W.; Zhang, J. W.; Du, Q. L.; He, D. P. Graphene-based integrated radiation heat-dissipation reconfigurable polarization conversion metasurface. *Nano Res.* **2024**, *18*, 94907494.

[18] Khan, M.; Han, C.; Li, H.; Dong, B. Q.; Li, D. Y.; Khan, Z.; Hu, H. T.; Sun, J. W.; Ni, W. H.; Lan, X. Single-particle insights into the

optical activity of planar-layered chiral plasmonic superstructures. *Nano Res.* **2025**, *18*, 94907416.
[19] O'Brien, M. N.; Jones, M. R.; Kohlstedt, K. L.; Schatz, G. C.; Mirkin, C. A. Uniform circular disks with synthetically tailorable diameters: Two-dimensional nanoparticles for plasmonics. *Nano Lett.* **2015**, *15*, 1012–1017.
[20] Hong, S.; Acapulco, J. A. I.; Jang, H. Y.; Park, S. Au nanodisk-core multishell nanoparticles: Synthetic method for controlling number of shells and intershell distance. *Chem. Mater.* **2014**, *26*, 3618–3623.
[21] Chen, L.; Ji, F.; Xu, Y.; He, L.; Mi, Y. F.; Bao, F.; Sun, B. Q.; Zhang, X. H.; Zhang, Q. High-yield seedless synthesis of triangular gold nanoplates through oxidative etching. *Nano Lett.* **2014**, *14*, 7201–7206.
[22] Scarabelli, L.; Coronado-Puchau, M.; Giner-Casares, J. J.; Langer, J.; Liz-Marzán, L. M. Monodisperse gold nanotriangles: Size control, large-scale self-assembly, and performance in surface-enhanced Raman scattering. *ACS Nano* **2014**, *8*, 5833–5842.
[23] Young, K. L.; Jones, M. R.; Zhang, J.; Macfarlane, R. J.; Esquivel-Sirvent, R.; Nap, R. J.; Wu, J. S.; Schatz, G. C.; Lee, B.; Mirkin, C. A. Assembly of reconfigurable one-dimensional colloidal superlattices due to a synergy of fundamental nanoscale forces. *Proc. Natl. Acad. Sci. USA* **2012**, *109*, 2240–2245.
[24] Lin, X. Y.; Ye, S. S.; Kong, C. C.; Webb, K.; Yi, C. L.; Zhang, S. Y.; Zhang, Q.; Fourkas, J. T.; Nie, Z. H. Polymeric ligand-mediated regioselective bonding of plasmonic nanoplates and nanospheres. *J. Am. Chem. Soc.* **2020**, *142*, 17282–17286.
[25] Lai, Y. H.; Cui, X. M.; Li, N. N.; Shao, L.; Zhang, W.; Wang, J. F.; Lin, H. Q. Asymmetric light scattering on heterodimers made of Au nanorods vertically standing on Au nanodisks. *Adv. Opt. Mater.* **2021**, *9*, 2001595.
[26] Hwang, Y.; Lee, S.; Kim, S.; Lin, J.; Yuan, X. C. Effects of Fano resonance on optical chirality of planar plasmonic nanodevices. *ACS Photonics* **2018**, *5*, 4538–4544.
[27] Jiang, L. Y.; Yin, T. T.; Dubrovkin, A. M.; Dong, Z. G.; Chen, Y. T.; Chen, W. J.; Yang, J. K. W.; Shen, Z. X. In-plane coherent control of plasmon resonances for plasmonic switching and encoding. *Light: Sci. Appl.* **2019**, *8*, 21.
[28] Lermusiaux, L.; Nisar, A.; Funston, A. M. Flexible synthesis of high-purity plasmonic assemblies. *Nano Res.* **2021**, *14*, 635–645.
[29] Zhou, Y. H.; Dong, J. Y.; Zhou, C.; Wang, Q. B. Finite assembly of three-dimensional DNA hierarchical nanoarchitectures through orthogonal and directional bonding. *Angew. Chem., Int. Ed.* **2022**, *61*, e202116416.
[30] Li, G. Z.; Chen, C. Y.; Li, Y. Y.; Wang, B.; Wen, J. L.; Guo, M. Y.; Chen, M.; Zhang, X. B.; Ke, G. L. DNA-origami-based precise molecule assembly and their biological applications. *Nano Lett.* **2024**, *24*, 11335–11348.
[31] Ding, L. J.; Ma, W. H.; Chen, X. L.; Wang, H. Z.; Song, H. T.; Fan, C. H.; Liu, X. G.; Yao, G. B. Prescribing DNA origami barrel-directed subtractive patterning of nanoparticles for crystalline superstructure assembly. *Angew. Chem., Int. Ed.* **2025**, *64*, e202424230.
[32] Long, L. Q.; Johnson, J. A.; Ren, R.; Michele, L. D.; Edel, J. B.; Ivanov, A. P. Reconfigurable DNA origami hinges for nanopore detection of microRNA. *Nano Res.* **2025**, *18*, 94907604.
[33] Li, Z. Y.; Li, M. Q.; Liu, X. G.; Chen, J. L. Design, regulation, and functionalization of self-assembled DNA crystals. *Nano Res.* **2025**, *18*, 94907250.
[34] Zhang, L.; Chu, M. G.; Ji, C. L.; Tan, J.; Yuan, Q. Preparation, applications, and challenges of functional DNA nanomaterials. *Nano Res.* **2023**, *16*, 3895–3912.
[35] Yin, X. H.; Schäferling, M.; Metzger, B.; Giessen, H. Interpreting chiral nanophotonic spectra: The plasmonic born-Kuhn model. *Nano Lett.* **2013**, *13*, 6238–6243.
[36] Auguié, B.; Alonso-Gómez, J. L.; Guerrero-Martínez, A.; Liz-Marzán, L. M. Fingers crossed: Optical activity of a chiral dimer of plasmonic nanorods. *J. Phys. Chem. Lett.* **2011**, *2*, 846–851.
[37] Wu, F.; Li, N.; Ding, B. Q.; Zhang, W. Plasmon-exciton strong coupling effects of the chiral hybrid nanostructures based on the plexcitonic born-Kuhn model. *ACS Photonics* **2023**, *10*, 1356–1366.
[38] González-Rubio, G.; Mosquera, J.; Kumar, V.; Pedrazo-Tardajos, A.; Llombart, P.; Solís, D. M.; Lobato, I.; Noya, E. G.; Guerrero-Martínez, A.; Taboada, J. M. et al. Micelle-directed chiral seeded growth on anisotropic gold nanocrystals. *Science* **2020**, *368*, 1472–1477.
[39] Chen, J. Q.; Gao, X. S.; Zheng, Q.; Liu, J. B.; Meng, D. J.; Li, H. Y.; Cai, R.; Fan, H. Z.; Ji, Y. L.; Wu, X. C. Bottom-up synthesis of helical plasmonic nanorods and their application in generating circularly polarized luminescence. *ACS Nano* **2021**, *15*, 15114–15122.
[40] Zhang, N. N.; Shen, Z. L.; Gao, S. Y.; Peng, F.; Cao, Z. J.; Wang, Y.; Wang, Z. Z.; Zhang, W.; Yang, Y.; Liu, K. et al. Synthesis and plasmonic chiroptical properties of double-helical gold nanorod enantiomers. *Adv. Opt. Mater.* **2023**, *11*, 2203119.
[41] Zhang, N. N.; Mychinko, M.; Gao, S. Y.; Yu, L. X. Z.; Shen, Z. L.; Wang, L.; Peng, F.; Wei, Z. L.; Wang, Z. Z.; Zhang, W. et al. Self-matching assembly of chiral gold nanoparticles leads to high optical asymmetry and sensitive detection of adenosine triphosphate. *Nano Lett.* **2024**, *24*, 13027–13036.
[42] Pan, J. H.; Wang, X. Y.; Zhang, J. J.; Zhang, Q.; Wang, Q. B.; Zhou, C. Chirally assembled plasmonic metamolecules from intrinsically chiral nanoparticles. *Nano Res.* **2022**, *15*, 9447–9453.
[43] Chang, H. H.; Murphy, C. J. Mini gold nanorods with tunable plasmonic peaks beyond 1000 nm. *Chem. Mater.* **2018**, *30*, 1427–1435.
[44] Nikoobakht, B.; El-Sayed, M. A. Preparation and growth mechanism of gold nanorods (NRs) using seed-mediated growth method. *Chem. Mater.* **2003**, *15*, 1957–1962.
[45] Hao, Y.; Li, Y. J.; Song, L.; Deng, Z. X. Flash synthesis of spherical nucleic acids with record DNA density. *J. Am. Chem. Soc.* **2021**, *143*, 3065–3069.
[46] Tikhomirov, G.; Petersen, P.; Qian, L. L. Triangular DNA origami tilings. *J. Am. Chem. Soc.* **2018**, *140*, 17361–17364.
[47] Zhan, P. F.; Wen, T.; Wang, Z. G.; He, Y. B.; Shi, J.; Wang, T.; Liu, X. F.; Lu, G. W.; Ding, B. Q. DNA origami directed assembly of gold bowtie nanoantennas for single-molecule surface-enhanced Raman scattering. *Angew. Chem., Int. Ed.* **2018**, *57*, 2846–2850.
[48] Gao, Z.; Gao, F.; Zhang, Y. M.; Xu, H. Y.; Luo, Y.; Zhang, B. L. Forward/backward switching of plasmonic wave propagation using sign-reversal coupling. *Adv. Mater.* **2017**, *29*, 1700018.
[49] Saito, K.; Tatsuma, T. Chiral plasmonic nanostructures fabricated by circularly polarized light. *Nano Lett.* **2018**, *18*, 3209–3212.
[50] Hashiyada, S.; Narushima, T.; Okamoto, H. Local optical activity in achiral two-dimensional gold nanostructures. *J. Phys. Chem. C* **2014**, *118*, 22229–22233.
[51] Shen, X. B.; Zhan, P. F.; Kuzyk, A.; Liu, Q.; Asenjo-Garcia, A.; Zhang, H.; García de Abajo, F. J.; Govorov, A.; Ding, B. Q.; Liu, N. 3D plasmonic chiral colloids. *Nanoscale* **2014**, *6*, 2077–2081.